

We are IntechOpen, the world's leading publisher of Open Access books Built by scientists, for scientists

6,900

Open access books available

186,000

International authors and editors

200M

Downloads

Our authors are among the

154

Countries delivered to

TOP 1%

most cited scientists

12.2%

Contributors from top 500 universities



WEB OF SCIENCE™

Selection of our books indexed in the Book Citation Index
in Web of Science™ Core Collection (BKCI)

Interested in publishing with us?
Contact book.department@intechopen.com

Numbers displayed above are based on latest data collected.
For more information visit www.intechopen.com



Diffraction Grating Groove Metrology Using AFM & STM

Leonid I. Goray

Abstract

AFM & STM metrology has been around for a long time, and especially intense since it has been awarded by the Nobel Prize in Physics in 1986. Since then, many AFM & STM groove profile measurements on surface relief diffraction gratings have been presented. However, a wide review of the results of the use of AFM & STM methods for groove metrology of various surface relief gratings has not really been undertaken. The following problems are discussed in this chapter: the cantilever tip deconvolution, geometry, and radius; groove shapes and abrupt groove slopes; roughness; PSD functions; etc. Also, the author demonstrates comparisons with other widely-used metrology techniques and examples of AFM & STM data of bulk, coated, and multilayer-coated ruled, or holographic, or lithographic gratings having realistic groove profiles. These gratings were chosen because high quality efficiency data exists, in particular, for space gratings or/and X-ray gratings characterized by synchrotron radiation sources; and their groove profiles, together with random nanoroughness, were measured by AFM or STM to be included in rigorous efficiency and scattered light intensity calculus. In the present chapter, both the earlier published results and the recent, non-published yet results are described and discussed.

Keywords: diffraction grating, AFM, STM, groove profile metrology, surface nanoroughness, PSD function, RMS roughness, diffraction efficiency, X-rays

1. Introduction

Scanning Tunneling Microscopy (STM) and Atomic Force Microscopy (AFM) metrology as parts of more general Scanning Probe Microscopy has been around for a long time, and especially intense since it has been awarded by the Nobel Prize in Physics in 1986. In 1988, our team was one the first who designed, manufactured, and used the specialized scanning tunneling microscope to measure newly developed big-size surface-relief holographic diffraction gratings obtained in non-organic photoresist and having in an order lower roughness (**Figure 1**) [1]. For today, STM & AFM profile measurements on surface-relief diffraction gratings are presented as a matter of routine, see, e.g., in Refs [2, 3]. On the other side, precise microscopic surface-relief patterns are used as grating standards to calibrate atomic force microscopes (see, i.e., in [4]).

However, a wide analysis of the use of the STM and AFM methods for surface relief grating groove metrology has not really been undertaken in details. The following problems are discussed here: the tip deconvolution, geometry, and radius; groove shapes and abrupt groove slopes; roughness; PSD functions; other. The

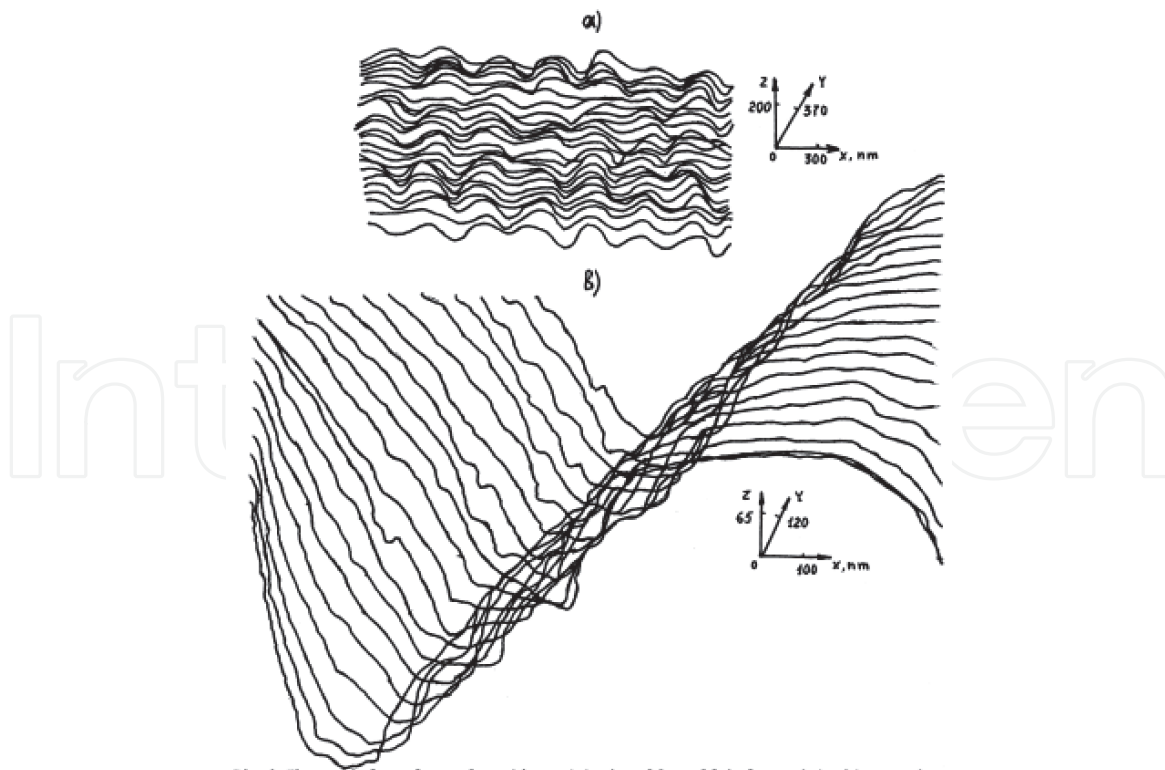


Figure 1.

STM images of holographic relief grating surfaces (Au-coated) obtained by (a) organic and (b) non-organic photoresists (after [1]).

author demonstrates examples of AFM & STM data and comparisons with other widely-used metrology techniques for bulk, coated, and multilayer-coated ruled, or holographic, or laser-lithographic, or electron-lithographic gratings having lamellar, or sinusoidal, or blazed, or other realistic groove profiles. These gratings were chosen because high quality efficiency data exists, in particular, for flight gratings or/and X-ray gratings characterized by synchrotron radiation sources; and their groove profiles, together with random nanoroughness, were measured by AFM or STM to be included in rigorous efficiency and scattered light intensity calculus.

Here the author briefly compares various standard techniques for exact determining the digital profile and 3D topography of a surface relief grating. Several widely used direct (or semi-direct – ‘imaging’) methods and respective instruments applicable for this purpose are compared. The advantage of using direct and exact groove metrology to predict efficiency and polarization characteristics of gratings now is well-known and widely used. The main purpose of such modern approach is rejecting unusable samples on earlier stages and decreasing expenses for their production and research. This is much more effective in compare to the earlier approaches, wherein: (1) a master grating is fabricated, whether by mechanical burnishing with a ruling engine, or holographic writing (interferometry), or direct laser recording (DWL), or various newer writing techniques, like as electron-beam lithography (EBL) and Si-etching, or their combinations; then, (2) it is replicated or/and coated, and, finally, (3) tested for the diffraction efficiency and scattering light intensity. For mechanically ruled gratings, a ‘test’ ruling can quickly be checked with this approach, whereas a complete ruling sometimes requires several days or even weeks of continuous use of expensive ruling machines [5]. Even for holographic or EBL gratings, considerable efforts of writing, etching and coating the grating with specialized coatings, especially multilayer coatings, can be decreased additionally if metrology validates that an intermediate product is suitable in the planned application.

2. Direct metrology techniques

The author briefly discusses and compares in the first part of this chapter several basic, among many others, direct metrology techniques: microinterferometry (as one of optical methods) [6], stylus (mechanical) profilometry [7], scanning electron microscopy (SEM) [8], and AFM [9]. Several examples of groove metrology results are presented and discussed further including those obtained very recently.

Any method for measuring the profile of a surface relief grating requires some calibration procedure [10]. The considered here methods are also widely used for surface microroughness determination on a nanometer or sub-nanometer level. Measuring main groove parameters of a grating, in particular, the actual groove depth or blaze angle, adds to the requirements for the specific metrology method. The depth of the groove profile, defined depending on the accuracy of a vertical calibration, basically determine the wavelength for the peak efficiency in a given optical mounting geometry (classical or conical) [11]. The common error of the order of a few percent in the lateral calibration can affect the prediction of the blaze wavelength that should be within hard tolerance for many practical applications. This is because the groove vertical geometry is often expressed relatively to the grating period, in dimensionless units. Any lateral error becomes vertical error in the respective topographical transformation. Fortunately, lateral errors can be fairly determined because the grating period is well known beforehand with high accuracy and, thus, the grating data itself gives a calibration factor to correct the lateral scale unit. The accurate lateral calibration is also required for rigorous efficiency modeling codes, in which the use of the average groove profile shape is very important to obtain exact efficiency data in all significant diffraction orders.

The microinterferometer is sometimes called as ‘optical profilometer’. It is essentially an interferometric head on a microscope, where the reference arm of the interferometer views a small, highly polished reference plate [6]. Such a reference can be removed from the results of measurements on highly polished surfaces that is important for grating measurements because many state-of-the-art gratings, especially for X-ray and Extreme Ultraviolet (EUV) applications, have the root-mean-square (RMS) roughness of the same order as the best reference plates. A Phase Shift Instruments model MicroXAM [12] has been used in the discussed work [10]. It has variable magnification from 2× to 100×; values of range and resolution for the 50× magnification is listed in **Table 1**. The instrument uses the zero path difference calculations independently for each pixel from a series of images obtained during a vertical sweep. This increases the available vertical range and the available slope angle range substantially, however any microinterferometer has two lateral resolution-restricted factors, which are not limitations in the other

Instrument	Microinterferometer 50×	Stylus profilometer	Atomic-force microscope	Units
Vertical resolution	0.05	0.1	0.05	nm
Vertical range	100	130	~5	μm
Lateral resolution	~0.3	~0.3	0.015	μm
Lateral range	163 (more w/stitching)	> 25000	100	μm
Limiting factor(s) for lateral resolution	MTF, sampling, need for retroreflection over the whole profile	Tip radius & angle	Tip radius	
Upper slope limit	–	45	~70	deg.

Table 1.
Measurement characteristics of three surface profiling instruments (after [10]).

considered methods. Namely, the optical resolution is due to the diffraction limit and pixel sampling is due to different magnifications and focusing. The theoretical limit on lateral resolution in such instruments is a half of the working wavelength, or, typically, about 0.1–0.3 μm . Thus, this method generally is not suitable to measure high-frequency (short-period) and/or low-depth diffraction grating.

The stylus profilometer has a diamond tip brought into direct contact with the surface, with calibrated contact force. As the tip moves across the surface, the motion of the tip is amplified, filtered, and detected. The basic limits inherent to such metrology devices are well-discussed, e.g., in [7]. Care must be exercised to prevent indentations of the surface by the tip, depending on materials and forces used, as well as accounting the tip size. The model used in this work is a Tencor P-10 [13]. **Table 1** presents the basic lateral and vertical ranges and resolutions typical for the instrument. Typical measurement parameters are: the tip radius of 0.1 μm (in the plane of dispersion), the tip speed of 5 $\mu\text{m/s}$, the digital sampling of 2 kHz, the tip force of 0.25 mg, and profile lengths of at least 100 μm (depending on the groove period). Note that in the last model of this instrument, KLA-Tencor HRP-260, the tip radius can be up to 25 nm and it has a high-resolution stage that produces scanning results similar to an AFM device. In the recent investigation we have used another model, namely, XP-1 Stylus (Ambios Technology, USA) [14].

The AFM instrument model that has been used in the discussed earlier work was a Digital Instruments Nanoscope III [15]. The recent investigation was carried out using the atomic-force microscope model NT-MDT NTEGRA Aura [16]. NTEGRA Aura is a Scanning Probe Microscope for studies in the conditions of controlled environment and low vacuum. The Q-factor of the cantilever in vacuum increases, thus gaining the sensitivity, reliability and accuracy of ‘probe-sample’ light forces measurements. At that, the change from atmosphere pressure to 10^{-3} Torr vacuum provides the tenfold gain of Q-factor. By further vacuum pumping, Q-factor reaches its plateau and changes insignificantly. Thus, NTEGRA Aura comparing to the high-vacuum devices it needs much less time, about a minute, to get the vacuum that is needed for the tenfold Q-factor increase. NTEGRA Aura has built-in closed loop control for all the axes, optical system with 1 μm resolution and ability to work with more than 40 different AFM regimes.

We have used for the Si-grating technology investigation a flexible Carl Zeiss SUPRA 25 SEM system with a versatile analytical specimen chamber that can be easily expanded with a choice of optional detectors and a full range of accessories [17]. Utilizing the unique GEMINI field emission column, it delivers superb resolution over the complete high voltage range with the magnification of up to 500000. The large 5-axes motorized cartesian stage is particularly useful for handling a number of smaller specimens simultaneously. It is equally useful for accommodating bulky or irregular shaped specimens.

Table 1 summarizes the capabilities and limits of the three metrology devices, which have been characterized earlier for grating metrology. As one can see, the atomic-force microscope has the finest lateral and perfect vertical resolutions. The stylus profilometer and the microinterferometer have comparable vertical ranges, however, without a possibility to determine superfine (atomic-scale) structures, i.e., nanoroughness, and abrupt slopes (see, e.g., **Figures 3–5**). On the other hand, the stylus profilometer has significantly larger lateral range for probing to the millimeter spatial range. Also, the AFM data gives a typical example of non-linearity that should be accounted and described further.

In the groove profile experiment, a series of step height calibration standards [18] has been used [10]. The vertical axis was calibrated using one of the smallest steps of 10 nm. Then the rest of the step height series was measured. Small errors, up to 8%, were observed for heights much higher than that used to calibrate the atomic-force

microscope. The fit to correct such nonlinearity was used when the nonlinearity gives a significant difference. The obtained results are summarized in **Table 2**.

In the manufacture and analysis of diffraction gratings, it is necessary to control certain of their parameters at each stage of the process. A SEM research [19] is permissible only at the stage of development of the manufacturing technology, because after each technological operation, see, e.g., [20] or Section 4.5, the sample of the Si-etched grating becomes less and less, since a fragment is separated from the sample to obtain a SEM image of a transverse cleavage (CS). In contrast to this, AFM studies are non-destructive; therefore, control of parameters in the manufacture of gratings is usually carried out with the help of AFM. We made a comparison between AFM (NTEGRA Aura microscope) topographies and SEM (SUPRA 25 system) images of Si-etched grating samples with the period of 2 μm . **Table 3** shows the results of AFM and SEM investigations of Si-etched gratings obtained at different stages of their fabrication. Table also presents the numerical comparing between the AFM and SEM results of the measured groove geometric parameters for the samples studied. The calculated value of the blaze (working facet) angle from the SEM studies was obtained from the sine determined by dividing the experimental values of the groove depth by the width of the working facet.

To measure the roughness of Si(100) plates etched through a DWL mask in KOH and intended for developing the technology of manufacturing Si-etched

Nominal height, nm	Microinterferometer	Stylus profilometer	Atomic-force microscope
8.7	7.92	8.1	—
25.8	—	—	25.7
42.7	43.4	42.4	—
530	—	—	520
1046	—	—	1005
1590	—	—	1469
960	—	—	—
Note No.	3, 4	2	1

1. Nonlinear at $\sim 8\%$ at highest step when calibrated to a 10 nm step.
2. Using 0.1 μm tip, could not resolve depth of 3.3 μm period, AFM step height standard.
3. Used at $50\times$ magnification.
4. At $100\times$ did not have lateral resolution to see the 3 μm period samples tested using AFM.

Table 2.
Step height data (after [10]).

Sample No.	Groove depth, nm		Working facet width, nm		Working facet angle, deg.	
	SEM	AFM	SEM	AFM	SEM	AFM
1	151 (47)*	133 (38)*	1571	—	—	—
2	149 (37)*	141 (44)*	—	—	—	—
3	111	121	1630	1710	3.90	4.05
4	111	111	1603	1594	3.97	—
5	105	114	1590	1580	3.89	4.13

*Height of Si-nubs.

Table 3.
AFM and SEM data for blaze Si-etched gratings.

Sample No.	RMS roughness, nm			
	Non-etched field		Etched bottom	
	Profilometer	AFM	Profilometer	AFM
1	2.6	0.2	2.8	0.8
2	3.2	1.6	4.0	2.5
3	3.4	0.2	4.5	1.8
4	2.8	1.7	2.9	4.9
5	2.4	1.5	3.5	4.3

Table 4.
AFM and stylus Profilometry data for Si-etched plates.

gratings, several high quality samples were selected using white light optical microscopy. The roughness of the etched bottom and the non-etched area was measured by two compared methods: Stylus Profilometry (XP-1 Stylus profilometer) and AFM (NTEGRA Aura microscope). Our studies were carried out on an atomic force microscope in the semi-contact or tapping mode; all scans had 512×512 points. We used TipsNano [4] silicon cantilevers with a typical radius of tips ~ 6 nm. The results of roughness measurement by two methods on topological elements (stripes) of $50 \mu\text{m}$ wide are presented in **Table 4**. As follows from the presented data, the RMS roughness obtained by different methods may differ by more than an order of magnitude. This is due to the radius of the stylus and the scanning length, which in that case were $2 \mu\text{m}$ and $80 \mu\text{m}$, respectively. However, this device is equipped with a stylus with a radius of $0.2 \mu\text{m}$, which, in principle, allows one to measure low- and mid-frequency gratings with smaller roughness. Note that for the etched bottom, where the average roughness is several times higher, the scatter of results is much smaller and ranges from several tens of percent to several times.

3. AFM groove metrology problems

A cantilever tip convolution, which limits the resolution of both the atomic-force microscope and the stylus profilometer, has been much studied and various algorithms to account for this effect has been developed and intensively used (see, e.g., [21] and also in this book). In the results presented in **Table 2** such algorithms have not be used. However, the general used rule is that the known tip radius should be much less than the measured periods of gratings. Typically, the radius of a fresh AFM cantilever tip is about $5\text{--}15$ nm; so, the rule of thumb is that for groove profiles of mid- and high-frequency gratings (say, periods of $100\text{--}300$ nm and less) tip deconvolution algorithms should be used. In the vertical direction, the depth parameter is smaller, and, apparently, the groove profiles recorded somewhat non-correctly for high-frequency gratings only. However, it depends also on absolute values of the groove profile depth, which can vary in two orders of magnitude.

Another important and general AFM problem, in particular for fine-structure gratings with steep slopes and high aspect ratios of grooves, is the shape and the radius of AFM cantilever tips. Tip size has the major impact on the resolution of images obtained by any atomic-force microscope. The knowledge of the tip radius and shape is essential for the quantitative interpretation of nano-scale lateral steps, in particular, for roughness having short correlation lengths. Tip wear is therefore a

key limitation in the application of AFM [22]. The results of nanoindentation experiments with diffraction gratings permanently confirm this conclusion. The measurement of the tip radius before and after measuring groove profiles of gratings was performed in Ref. [10], and they found that the radius to be in the range of 10–20 nm. One measurement found a fresh tip to be ~ 10 nm radius and a used one to be ~ 20 nm. Therefore, one should restrict an AFM-profiling work to gratings of period much longer than 10–20 nm, as it has been discussed above.

One more problem in AFM measurements of diffraction gratings is the grooves with steep facet slopes, which can be 80 degrees and more for echelle gratings [2]. This problem is similar to measurements of the rectangular (lamellar) groove profile in microelectronics [23]. To accurately measure such general trapezoidal profiles with steep or even negative sidewalls, a large change in the angle of inclination of a cantilever (or scanner, or sample) and/or special cantilever (tip) shape are required, as well as taking into account the aspect ratio of measured grooves [24]. Several studies applied to periodic structures demonstrate that some combination of the tilted probe, special orientations of AFM images and appropriate deconvolution algorithms allows the precise groove shape reconstruction at any aspect ratio [25]. An example of such problem successfully solved is the average groove profile (two grooves) of a 112/mm echelle R5 grating (blaze angle $\sim 78^\circ$) derived from AFM images and presented in **Figure 2**.

In **Figure 3**, typical power spectral density (PSD) 1D functions for Si(111) substrate and Si-etched grating samples (see also Section 4.5) are shown. An estimator of the PSD function is factually the periodogram for any periodic, or quasi-periodic, or random profile, or some combination. Assuming the ergodicity of a stochastic process connected with a random generation of asperities, the PSD function can be found as the Fourier transform of the autocorrelation function [26]. Although these functions are mathematically equivalent, one can analyze easily any corrugations of the profile shape simultaneously, i.e., random roughness and groove depth variations, using the 1D or 2D PSD function. Then, the RMS roughness is directly calculated through PSD as the root square of the integral over an effective range of allowed spatial frequencies. Thus, a wide lateral scanning range may require for an AFM instrument to take into account in the evaluated RMS roughness all spatial frequencies (or correlation lengths). It is especially important for low-frequency (long-period) gratings having additionally large correlation lengths of random roughnesses. A good discussion related to this problem and devoted of the use of AFM and similar instruments for measurements of PSD functions of smooth



Figure 2.
 Average AFM groove profile for 112/mm echelle R5 grating.

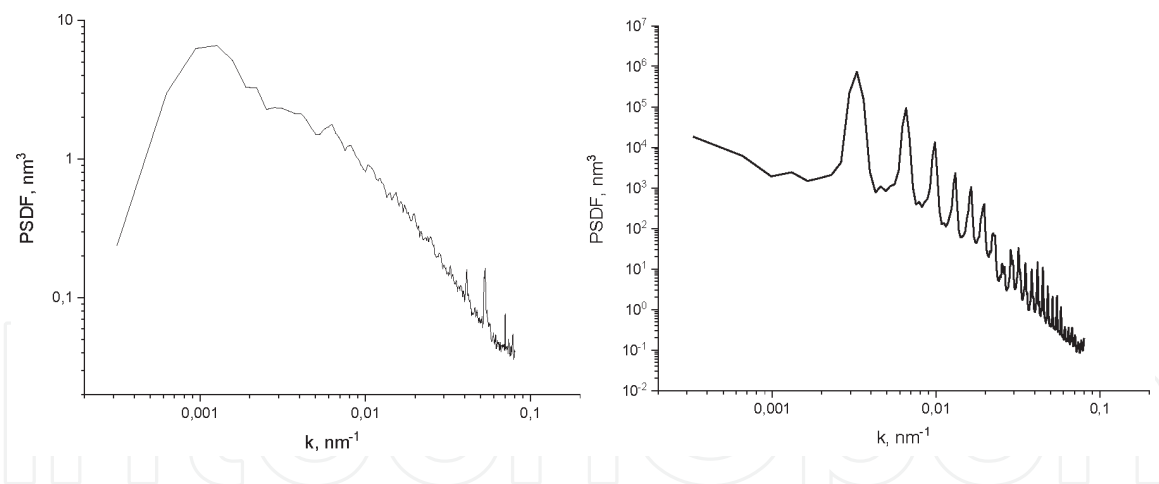


Figure 3.

PSD function: (left) for Si(111) substrate; (right) for Si-etched grating with 500/mm and 4° blaze angle.

mirrors for imaging systems working in the X-ray–EUV range can be found in [27]. So, if one need to use images with a scanning area of about $100 \times 100 \mu\text{m}^2$ then thermal drifts, hysteresis, and essential scanner nonlinearities should be accounted.

4. AFM groove metrology results

4.1 Space ruled grating for Visible: NIR

The abovementioned metrology techniques were applied to validate the efficiency of a chosen grating from an ordered grating set which is mounted in the Space Telescope Imaging Spectrograph (STIS) flown aboard the Hubble Space Telescope (HST) [28]. A – 1-order reflection grating with 67.556/mm blazed for 750 nm (1.44° nominal blaze angle) working in the range from 500 to 1000 nm at 8° incidence angle was chosen by us for a certification [29]. The pattern size was 1.5 inches by 1.5 inches, and the ruled area was 30 mm by 30 mm. A sister-replica to this grating, designated ‘Ng41M’ or by its manufacturers’ (Richardson Gratings of Newport Corp.) serial number, 1528, is in use on the HST/STIS as a red survey grating (blazed in the red visible and near infrared range) [10]. In its flight application, this grating had a reflective overcoating of 100 nm Al plus 25 nm MgF₂. However, in these wavelengths the effect of the MgF₂ layer is minor and simulations have showed no valuable difference, within a small part of the accuracy in the measured diffraction efficiency) with such coating or without it. This grating was chosen as an example because: (1) high quality efficiency data exists for it, including rigorous efficiency calculus using the realistic groove profile shape; and (2) groove profiles can be measurable by the mentioned above three methods for a direct comparison.

Portion of a trace of grating No. 1528 taken with the microinterferometer is shown in **Figure 4**. Both the depth and the profile shape are somewhat distorted in compare with the groove profiles in **Figures 5, 6** obtained by the other considered methods. However, as one can see, the overall groove depth and profile are evident. It is clear from the all figures that the profile roughness is higher on the upper sloped portion than on the steep edges. Difficulties in holding the sample steady during ‘flyback’ prevented reproducibility of measurements for that microinterferometric study.

The groove profile was characterized in details AFM measurements. The tips used here were 10 or 20 nm in radius. An example of the typical groove profile of No. 1528 grating is presented in **Figure 6**. **Figure 6** shows an example of AFM data

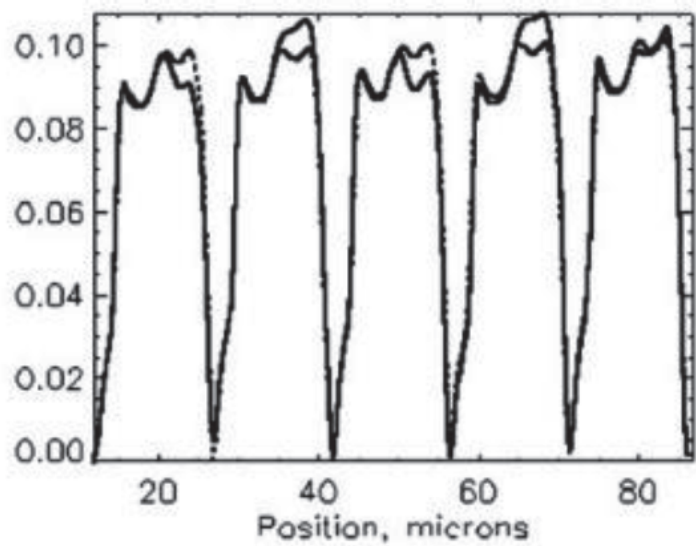


Figure 4.
Portion of a microinterferometer trace of ruled grating No. 1528 (after [10]).

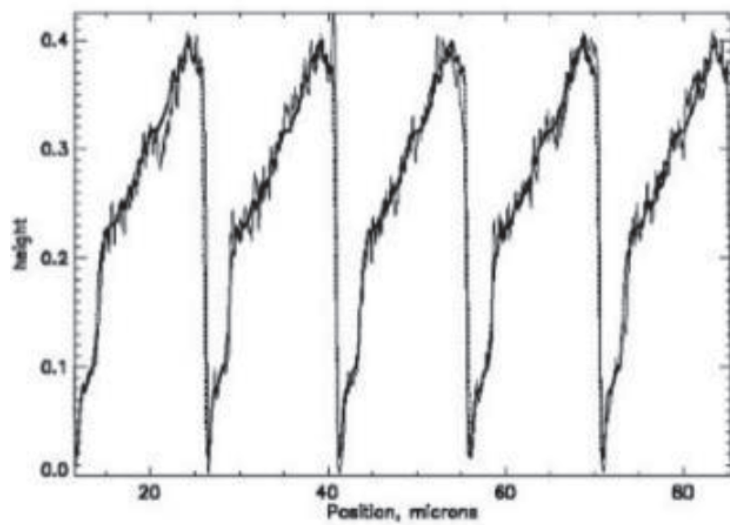


Figure 5.
Portion of a stylus profilometer trace of ruled grating No. 1528 (after [10]).

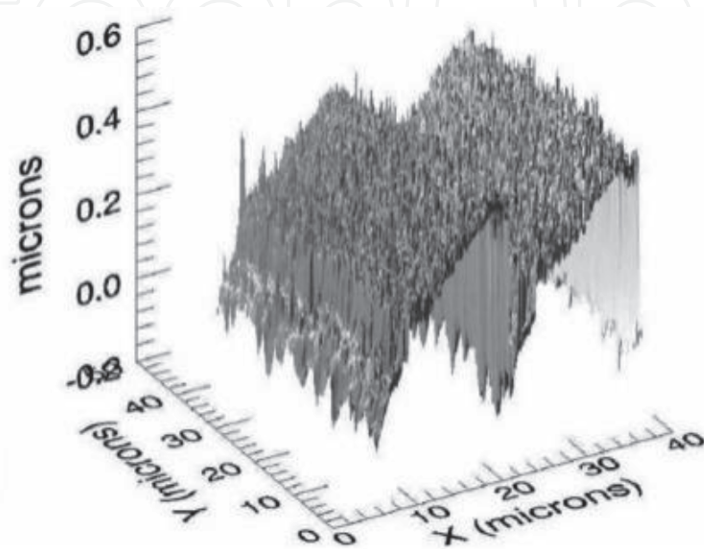


Figure 6.
AFM image of two grooves of ruled grating No. 1528 (after [10]).

for a portion of the surface of the investigated ruled grating. The basic groove profile shape is clearly evident, along with portions of the profile that are rougher than others, and some roughness along the grooves is indicated as well. **Figure 6** shows that the minimum of the grooves is clearly visible in the AFM image. If, as usually, one selects the bottom of the groove as the minimum value, there are two complete grooves in each scan.

The resulting average groove profile – with averaging performed both across the grooves and along as well – is shown in **Figure 7**. The solid line is based on the AFM data, and the dotted line is based on the stylus profilometer data: the groove tops are aligned for the purpose of this comparison; the relatively sharp groove bottom is not as well resolved by the stylus profilometer. The periodicity of the profile is shown by comparing a model of the averaged scan based on the average groove profile shape to the average scan. This is demonstrated by dotted lines plotted against the initial data in **Figure 4** (microinterferometer) and **Figure 5** (stylus profilometer). Once the average profile has been determined, the fitting routine finds the sawtooth and two-angle shape fits by the method of least squares. It is found in the considered case the blaze angle of 1.45° and the anti-blaze angle of 30° (**Figure 8**). The efficiency in general is fairly insensitive to the anti-blaze angle, and the fitting procedure does not fit it as consistently as it does a case of the blaze angle. Thus, the final average groove profile derived from AFM measurements for efficiency modeling purposes is shown in **Figure 8** with 100 discretization points [29].

4.2 Soft-X-ray: EUV blaze gratings

The surface of gratings, namely, the master [30] and replica [31] gratings, as examples of ‘good’ products, were characterized using a Topometrix Explorer Scanning Probe microscope [32], a type of atomic-force microscopes. The gratings have 2400/mm, a concave radius of curvature of 2.0 m, and a patterned area of size 45 mm by 35 mm. The master grating was fabricated by Spectrogon UK Limited (formerly Tayside Optical Technology). The groove pattern was developed in fused silica by a holographic technique using ion-beam etching to produce an approximately triangular, blazed groove profile. Ion-beam etching results in a groove profile much closer to triangular than the ideal blazed (sawtooth) profile with the apex angle of $\sim 90^\circ$. The master grating was uncoated. The replica of the master grating was produced by Hyperfine, Inc. As a result of the replication process, the replica grating had an aluminum surface. A thin SiO_2 coating was applied to the Al surface

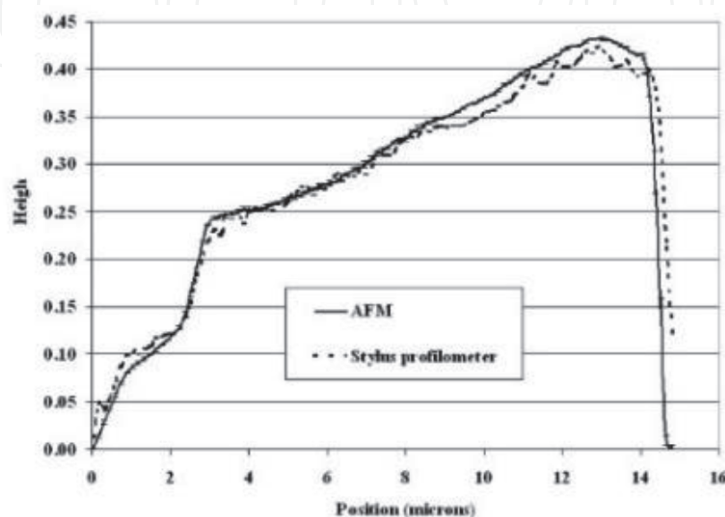


Figure 7.
Average groove profile for grating No. 1528 based on AFM and stylus profilometer data.

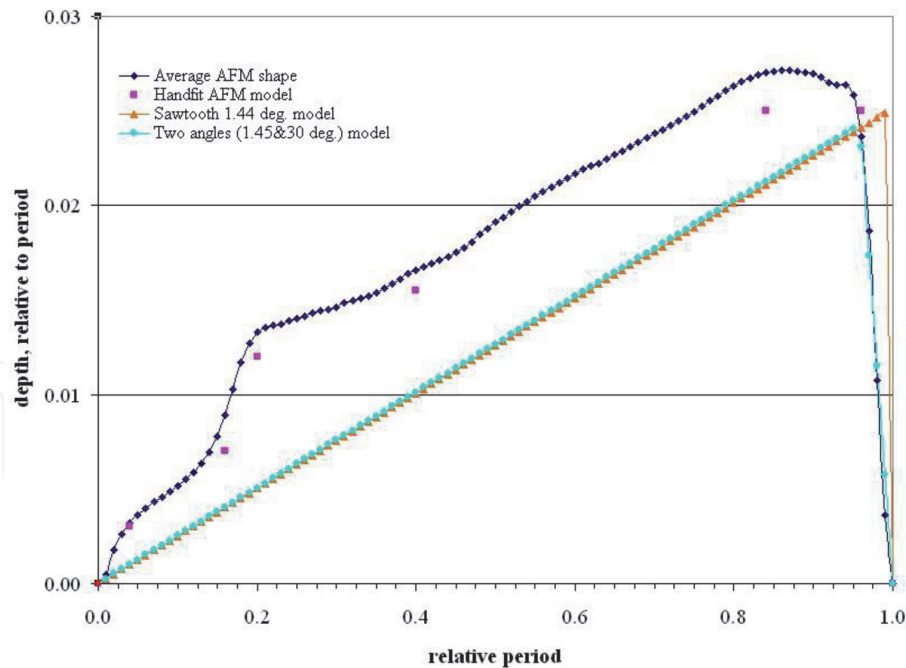


Figure 8.
 Models of normalized to period groove profiles of No. 1528 grating.

for the purpose of reducing the nanoroughness and protecting the surface from an additional oxidation.

The AFM images typically had 500×500 pixels and a scan range of 1 to 20 μm (pixel size 20 to 400 \AA). The silicon probe had a pyramid shape. The base of the pyramid was 3 to 6 μm in size, the height of the pyramid was 10 to 20 μm , and the height to base ratio was approximately 3. The tip of the pyramid had a radius of curvature 100 to 200 \AA . The AFM scans were performed using the non-contact resonating mode, where the change in the oscillation amplitude of the probe is sensed by the instrument. A surface topology reference sample was used to optimize the AFM scanning parameters, to calibrate the height scaling of the instrument, and to evaluate the performance of the AFM. This was essential for the accurate characterization of the gratings. The surface topology reference sample consisted of an array of approximately square holes fabricated on the silicon dioxide surface of a silicon die by VLSI Standards, Inc. [18]. The top surface of the die was coated with a thin layer of Pt. The hole array had a pitch of 3 μm and a hole depth of 180 \AA .

One typical AFM image of the master grating measured using 16- \AA pixels is shown in **Figure 9**, where the vertical scale has been scaled to reveal the texture of the groove surface. The RMS roughness, determined by integrating the PSD function over $2\text{--}40\ \mu\text{m}^{-1}$ range, was 3.2 \AA . Most of the roughness is concentrated at low spatial frequencies as is apparent from the analysis of the PSD function. The central portion of the AFM image shown in **Figure 9** that covers one period of the grating pattern was selected for further investigations. An analysis program was written in the Interactive Display Language (IDL) for this purpose and it is discussed in detail in Ref. [31].

The histogram of the pixel heights, for one period of the grating pattern, is shown in **Figure 10**. The maxima at 10 \AA and 85 \AA in **Figure 10** are caused by rounding of the groove profile at the peaks and the troughs which is a result of the pattern fabrication process. An ideal groove profile, either sawtooth or triangular, would have a flat height histogram. The separation between the peaks in **Figure 10** represents the average groove height, approximately 75 \AA . The local blaze angle at each pixel was determined by using a least squares algorithm to fit a linear curve to

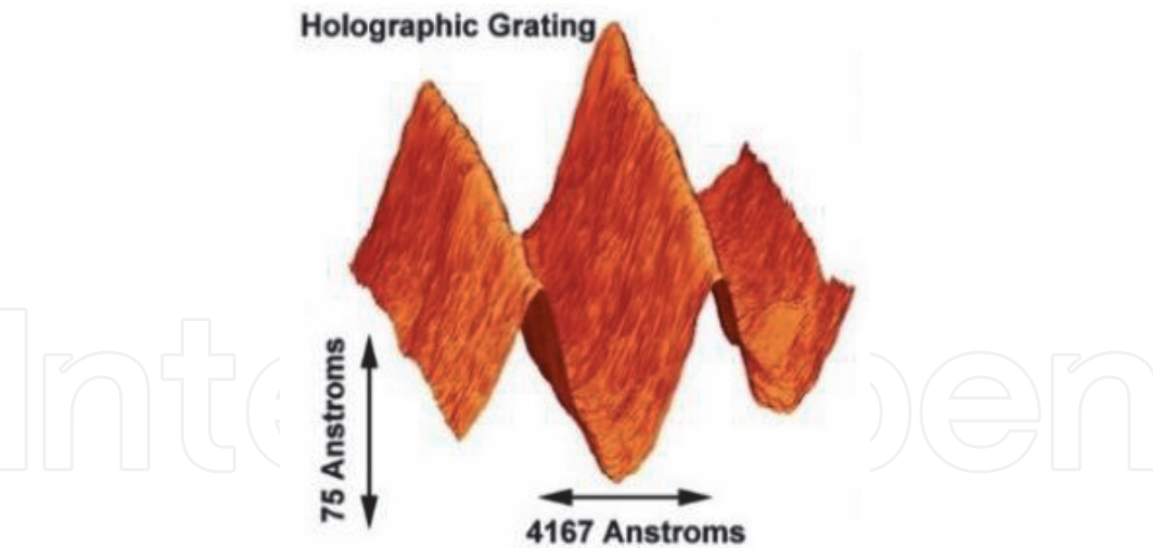


Figure 9.
AFM image of 2400/mm holographic (master) grating (after [30]).

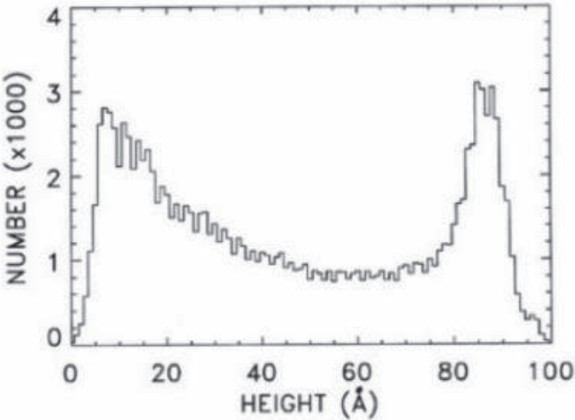


Figure 10.
Histogram of pixel heights from AFM image of 2400/mm holographic grating (after [30]).

the data points in a sliding window. The window was 25 pixels (400 Å) long in the direction perpendicular to the grooves and one pixel wide parallel to the grooves. The blaze angle is the arctangent of the fitted slope. The histogram of the blaze angles, for all rows of data in one period of the grating, is shown in **Figure 11**. The peak at 2.5 deg. represents the classical blaze angle, and the peak at 5.5 deg.

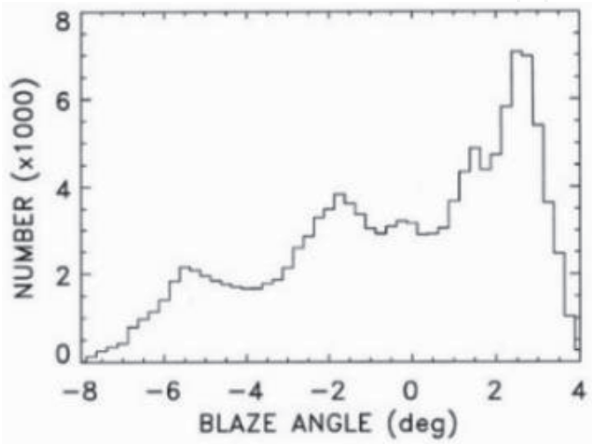


Figure 11.
Histogram of blaze angles from AFM image of 2400/mm holographic grating (after [30]).

represents the steep facet of the ideal sawtooth profile as modified by the ion-beam etching process. For a density of 2400/mm and for facet angles of 2.5 deg. and 5.5 deg., an ideal grating would have a groove height of 125 Å. However, the measured value of 75 Å (**Figure 10**) indicates a significant degree of rounding at the peaks and troughs of the groove profile. In addition, the measured ratio of the heights of the 2.5 deg. and 5.5 deg. features in the angle histogram (**Figure 11**) is approximately 3, greater than the ratio of approximately 2 that is expected based on the average facet angles.

The interpretation of the widths of the features in **Figure 11** is difficult because they are complicated functions of the surface roughness, the width of the sliding window, and the probe geometry. This is addressed in the publications [30, 33, 34]. The feature at -2 deg. in **Figure 11** results from the fits to the peaks and troughs of the groove profile, where the local slope is changing rapidly but has an average value near zero. Simulations show that the -2-deg offset of this feature from zero is a consequence of the unequal average blaze angles of the two facets. To provide a groove profile for the efficiency calculation, a representative AFM scan perpendicular to the grooves was chosen at random and scaled to the average groove height. The resulting groove profile is shown in **Figure 12**. This groove profile has 210 points.

An AFM image of two grooves of the replica grating is shown in **Figure 13**. The scan was performed across the grooves over a range of 1 µm (20-Å pixels). The vertical scale in **Figure 13** has been expanded to reveal the texture the texture of the grating surface. The PSD function derived from a 2 µm-size image spanning nearly 5 grooves is shown in **Figure 14**. The peak in the 2 to 3 µm⁻¹ frequency range results from the 0.4167 µm groove period. The RMS roughness is 7 Å in the 4–40 µm⁻¹

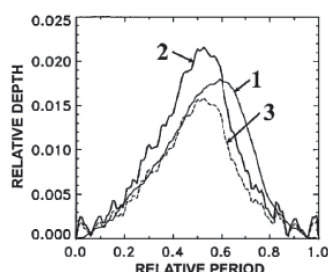


Figure 12.
 Average groove profile from AFM image of 2400/mm grating: (1) 7.5-nm-deep master; (2) 9.0-nm-deep replica; (3) 6.6-nm-deep scaled replica (after [35]).

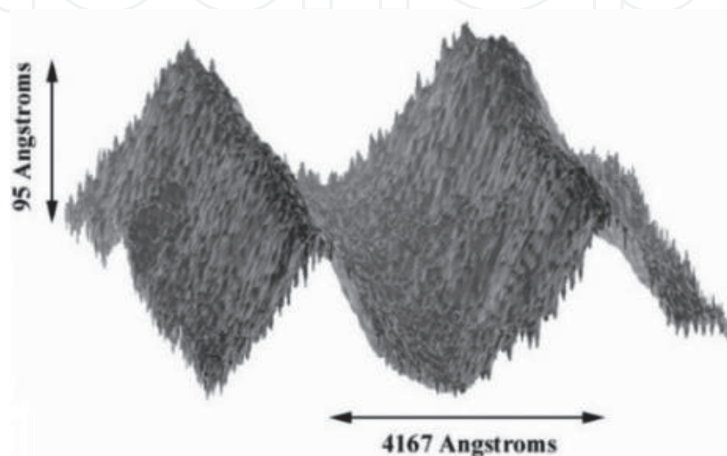


Figure 13.
 AFM image of 2400/mm replica grating (after [31]).

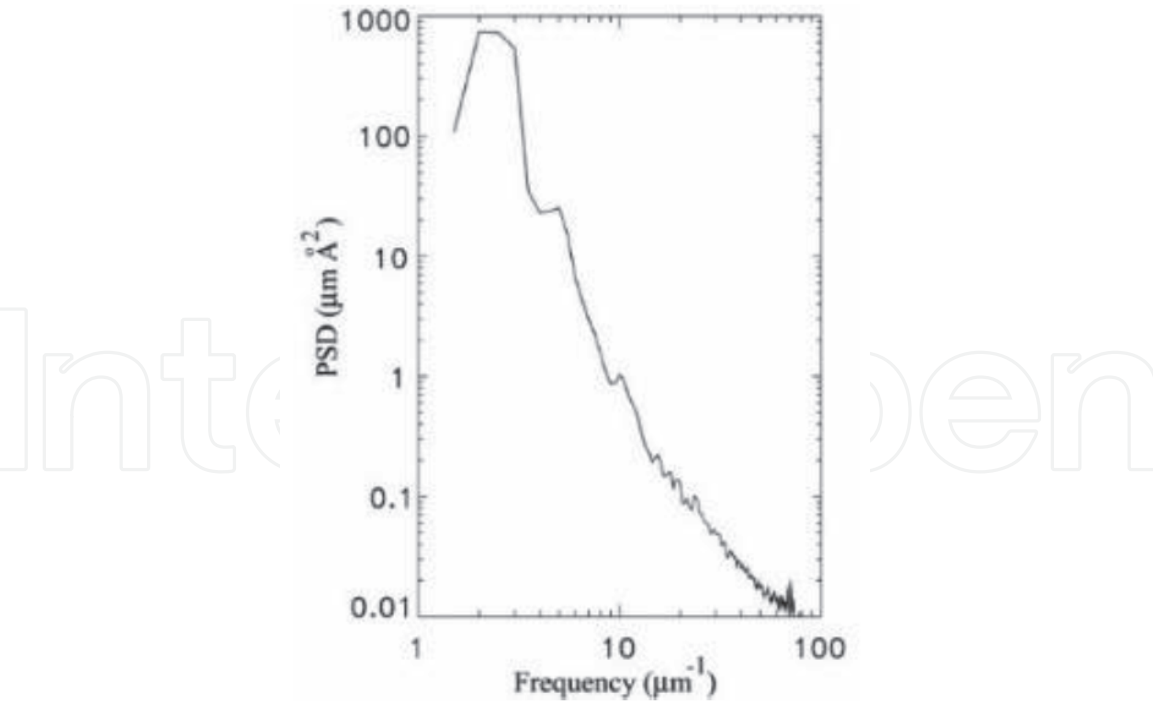


Figure 14.
PSD function of 2400/mm replica grating from AFM image (after [31]).

frequency range. By comparison, the RMS roughness of the master grating measured by the same type of AFM instrument was 3.2 Å, and this implies that the replica grating is significantly rougher than the master grating. This may result from the replication process, which for a concave grating is at least a two-step process. Furthermore, the master grating was fabricated on a fused silica surface by a holographic technique and was ion-beam polished, while the Al surface of the replica grating may contribute to its larger nanoroughness. The replica grating without the SiO₂ coating was not characterized by AFM. Typical average groove profile derived from the AFM image (1 μm in size) of the replica grating is shown in **Figure 15**. The groove profile is approximately triangular in shape with rounded corners and troughs and with facet angles of 3.4 deg. and 6.2 deg. The average groove depths derived from the AFM images are in the range 85 to 95 Å. These values of the facet angles and the groove depth are larger than the corresponding values for the master grating, 2.5 deg. and 5.5 deg. facet angles and 75 Å average groove depth (**Figure 12**). Thus, the grooves of the replica grating are deeper and the facet angles are steeper compared to those of the master grating.

Multilayer gratings were produced by application of Mo₄Ru₆/Be multilayer coatings [35, 36] to two replicas of the described holographic master grating.

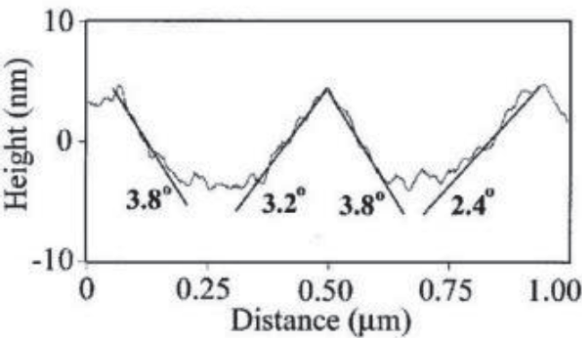


Figure 15.
Average groove profile from AFM image of 2400/mm Mo₄Ru₆/Be grating (after [36]).

Beryllium-based multilayer coatings can provide substantial reflectance at wavelengths near 11 nm. Such a Mo₄Ru₆/Be multilayer coating with 50 bi-layers was applied to the grating substrate. The coating was deposited by the magnetron-sputtering technique. Here we describe one of the multilayer gratings.

The surface of the multilayer grating was also characterized using the same Topometrix Explorer scanning probe microscope. The grating topography was measured merely for the master, replica, and multilayer gratings. The scan was performed across the grooves over a range of 1 μm (2-nm pixels). Typical groove profiles derived from the AFM image (1 μm in size) of the master, replica, and multilayer gratings are shown in **Figures 9, 13, 15**, respectively. These groove profiles have from 120 to 210 points. The groove profiles are approximately triangular in shape with rounded corners and troughs and with facet angles of 2.5° & 5.5°, 3.4° & 6.2°, and 3.0° & 4.1°, respectively. The average groove depths derived from the AFM images are in the range 7 to 8 nm, 8.5 to 9.5 nm, and 8 to 9 nm, respectively. Within the AFM groove-to-groove variation of the facet angles, the border shapes did not significantly change after multilayer coating. As determined above the average surface of the multilayer grating was characterized using a scaled replica AFM profile (**Figure 12**).

4.3 Space holographic gratings for VUV: NUV

The aforementioned AFM method was applied to simulate the efficiency of a 5870/mm G185M grating intended for operation at vacuum-ultraviolet (VUV) wavelengths below 200 nm [37]. This grating has the highest groove density and the shortest operational wavelength range of all Cosmic Origins Spectrograph (COS) gratings planned for the last servicing mission to the HST [38]. The G185M master grating was recorded holographically on 40 mm by 15 mm rectangular fused silica blank and the Pt coated at HORIBA Jobin Yvon Inc. [3]. An adhesive Cr coating, a working Al coating, and a protective (from oxidation) MgF₂ coating were deposited on Au-coated replica gratings at NASA/GSFC.

Resonance efficiency anomalies associated with waveguide funneling modes inside the MgF₂ dielectric layer degrading the G185M COS NUV grating performance were measured and qualitatively described at NASA/GSFC [39]. We used PCGrate-SX v. 6.1 [40] to model the efficiency of the G185M subwavelength grating with real boundary profiles (measured by AFM) and refractive indices (RIs) taken from different sources, including best fits of the calculated efficiency data to experimental ones [37].

The border profiles were characterized using AFM measurements. The profile of the G185M grating (replica C) intended for operation in the 170–200-nm range was AFM-measured before and after deposition of the Cr/Al/MgF₂ coating (**Figure 16**). As seen from the figure, after the deposition the profile depth decreased by about a

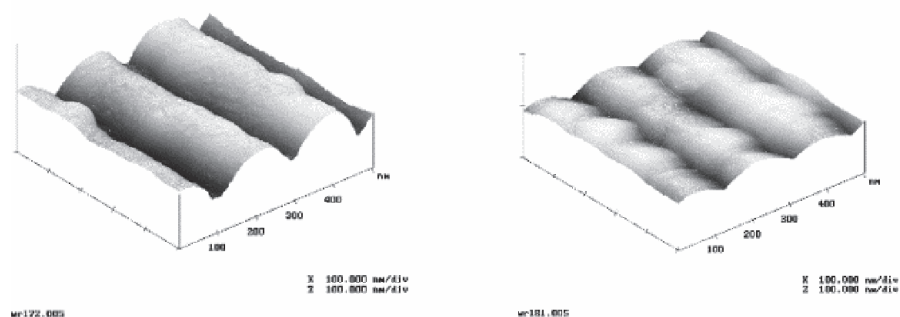


Figure 16.
 G185M AFM-measured surfaces before (left) and after (right) coating Al plus MgF₂ (after [37]).

factor of 2.05 (46.4 nm against 22.6 nm), and the profile shape changed noticeably too, thus evidencing the case of nonconformal layering of the grating. For the reason that all G185M gratings were manufactured from the same master and by the same technology, one may suggest that all of them share before- and after-coating profiles. The average before-coating groove profile had 165 points and the average after-coating profile had 163 points.

To determine which of the two AFM-measured boundary profiles, MgF₂ (border profile 1 measured after Cr/Al/MgF₂ coating) or (Cr)-Au (border profile 2 measured before Cr/Al/MgF₂ coating), is closer to the MgF₂-Al boundary, we started with modeling the non-polarized (NP) efficiency of a two-boundary grating. We assume a conformal MgF₂ layer (the lower MgF₂-Al boundary is identical in shape to the MgF₂ one) with the 40.1 nm thickness. The calculated efficiencies (**Figure 17**, pink curve) differ from the measured values in time throughout the whole wavelength range, thus implying invalidity of a model with a conformal layer. All calculated efficiency data presented in **Figure 17** were obtained with the RIs of Al and MgF₂ taken from the handbook of Palik [41]. Although hereinafter the experimental efficiency data of two grating replicas (A and B) are displayed, we will focus primarily on discussing the grating A data (solid dark blue squares in **Figure 17**), because replica A is the grating on which more measurements were performed.

The next step is to use two models with nonconformal layers, one with the lower boundary being the same as border 2 (**Figure 17**, yellow curve) and the other with the boundary scaled from border 2 at all points by a factor of 0.488 to the profile depth of border 1 (**Figure 17**, bright green curve). In both cases, a vertical displacement of one boundary with respect to the other (shift of the boundary reference levels) was 40.1 nm, as in the conformal model. As evident from **Figure 17**, the nonconformal model with unscaled lower boundary yields a noticeably superior qualitative agreement with experimental data. This suggests that the MgF₂-Al boundary more closely resembles border profile 2 than border profile 1. The model takes into account the fact that the thickness difference of 23.8 nm between the lower and upper boundaries should be added to the conformal vertical displacement (40.1 nm) to obtain an adequate vertical displacement for the nonconformal MgF₂

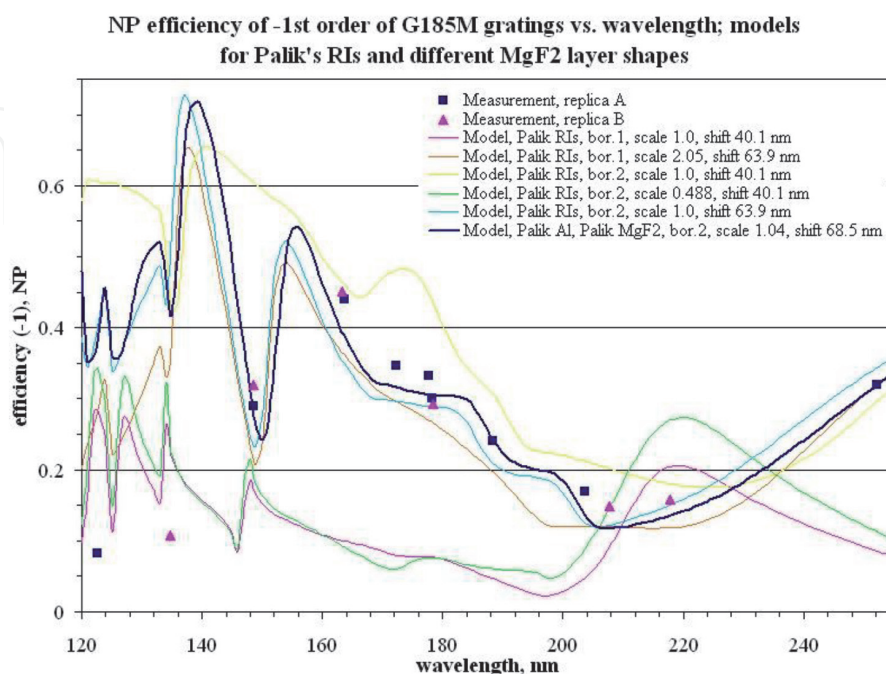


Figure 17.
G185M -1st-order NP efficiency measured and calculated for different layer shapes.

layer. In this way the period-averaged thickness of the nonconformal MgF_2 layer is kept approximately equal to 40.1 nm within the boundary shape distortion.

To determine the effect of profile shape, we set up models with equal depths and vertical shifts. The first one has border 1 scaled to the depth of border 2 (making it grater by a factor of 2.05) and a vertical displacement between the zero boundary levels equal to 63.9 nm. As seen from **Figure 17**, the efficiency of this model (orange curve) is close to that of another model with unscaled border 2 and a vertical shift of 63.9 nm (sky blue curve), while it is inferior by 40% or more as far as matching the experimental efficiencies. The latter suggests that, to set up an exact model, one has not only to determine the depth of the MgF_2 -Al boundary but also to take into account the shape of its profile – see **Figure 18**.

Having determined the type of the MgF_2 -Al boundary profile, we have to refine it by scaling the shape in depth and then comparing the efficiencies obtained for each model with experimental data. Another fitting parameter is the vertical displacement of the boundaries. By automatic modeling of the efficiency over a small-meshed grid of these two parameters and wavelength, one can determine the average thickness of the MgF_2 layer from the best fit between the calculated and the experimental efficiencies. Even slight changes (with a few nanometers) in profile depth and vertical displacement give a noticeable rise to the efficiency at fixed wavelengths, particularly in resonance regions. **Figure 17** presents an efficiency curve (heavy dark blue) for the model with a lower-boundary scaling factor of 1.04 and a vertical displacement of 68.5 nm. The model with these parameters of the layer geometry provides the better least-squares fit (not worse than 20%) of calculated efficiency to experimental data, both in the medium and in the long-wavelength ranges. As to the short-wavelength part, no variations in the lower boundary profile chosen within our approach yield theoretical values of the efficiency close enough to the measured ones.

What only remains is to check whether the average-thickness parameters of the MgF_2 nonconformal layer used in the final model provide a better fit between the calculated and experimental values of efficiency throughout the wavelength range with a new MgF_2 RI library (Keski-Kuha-Goray) [37]. To do this, we scale the vertical displacement and boundary parameters for the final model. Graphical results of this three-parameter optimization (scale, shift, and wavelength) are displayed in **Figure 19**. The final geometrical model of border shapes and layer thicknesses is demonstrated in **Figure 18**. The optimization procedure using different thicknesses for all the layers accounted has been applied using the least-square method. An analysis of these results shows that the parameters of the final model do

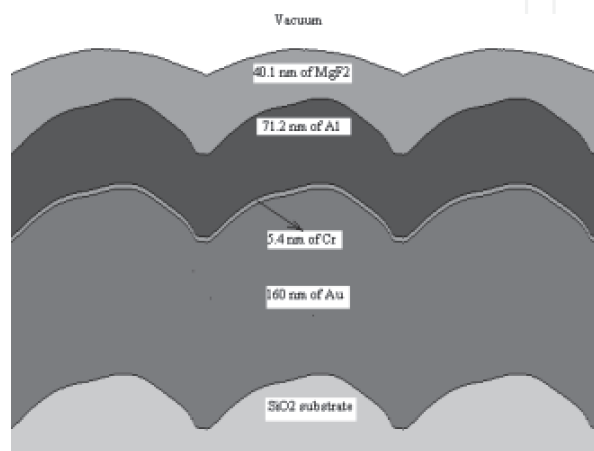


Figure 18.
 Average G185M AFM border profiles before and after coating Cr/Al/ MgF_2 .

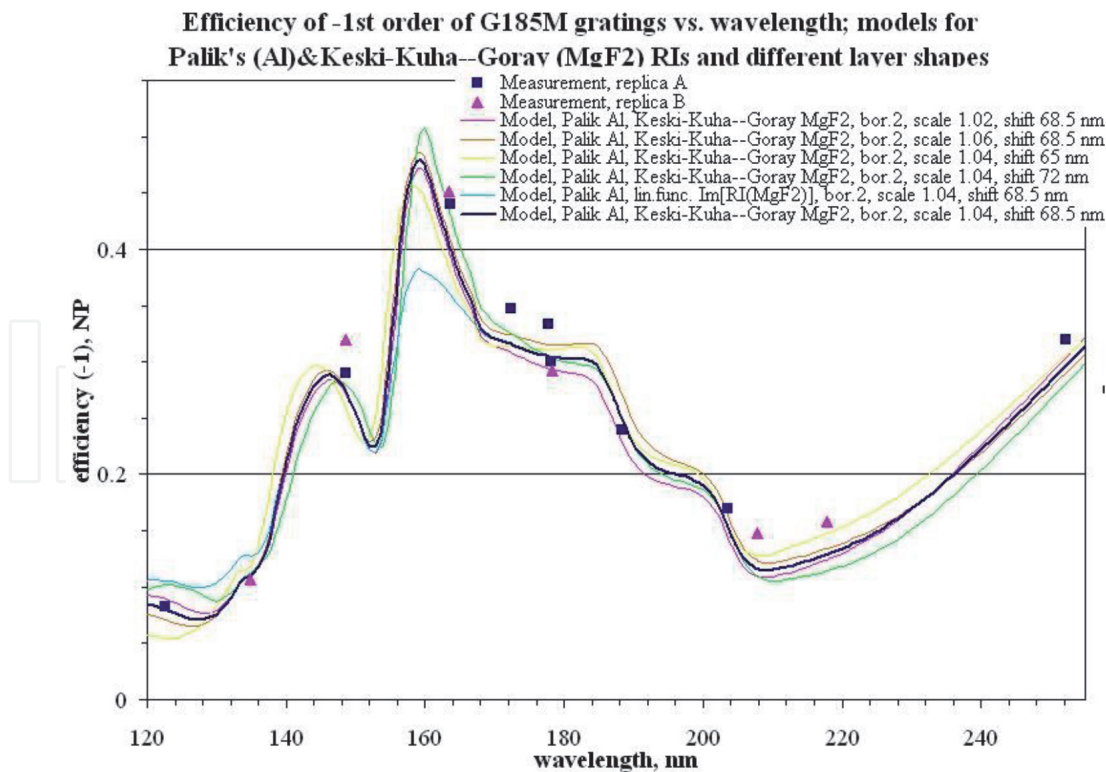


Figure 19.

Five-boundary G185M grating model. Horizontal and vertical scales are different (after [37]).

indeed provide the best agreement between the measured and calculated values of efficiency throughout the wavelength range. The relative deviation of experiment from theory for all wavelengths at which grating A was studied does not exceed 10% throughout the wavelength range. **Figure 21** presents also an efficiency curve (sky blue curve) calculated by use of the approximate values of the MgF_2 absorption index; all other parameters of the final model remain intact. A comparison of the curve efficiencies based on scaled (sky blue curve) and exactly calculated (heavy dark blue curve) values of absorption shows that the efficiency changes at the wavelengths where the RI imaginary values scale only slightly are indeed appreciable.

4.4 Imprinted off-plane blaze grating for soft X-rays

Grazing-incidence off-plane gratings have been suggested for the International X-ray Observatory (IXO) [42]. Compared with gratings in the classical in-plane mount, X-ray gratings in the off-plane mount have the potential for superior resolution and efficiency for the IXO mission [43]. The results of efficiency calculations for such a 5000/mm gold-blazed soft-X-ray grating in a conical (off-plane) mount using the average groove profile derived from AFM measurements was presented in [44].

An AFM study of the grooved area confirmed the larger than expected blaze angle. The AFM scans across the grooves near the center of the grating are shown in **Figure 20(a)**, where each scan is displaced vertically by 1 nm for ease of viewing. The standard deviation of the data points from the average scan curve is 0.89 nm and is a measure of the roughness of the groove profile. The histogram of the angles between each pair of scan points is shown in **Figure 20(b)**, where a Gaussian curve is fitted to the angle distribution. The top corners of the groove profiles are rounded, and this results in a rather broad distribution of angles with a centroid value of 13° .

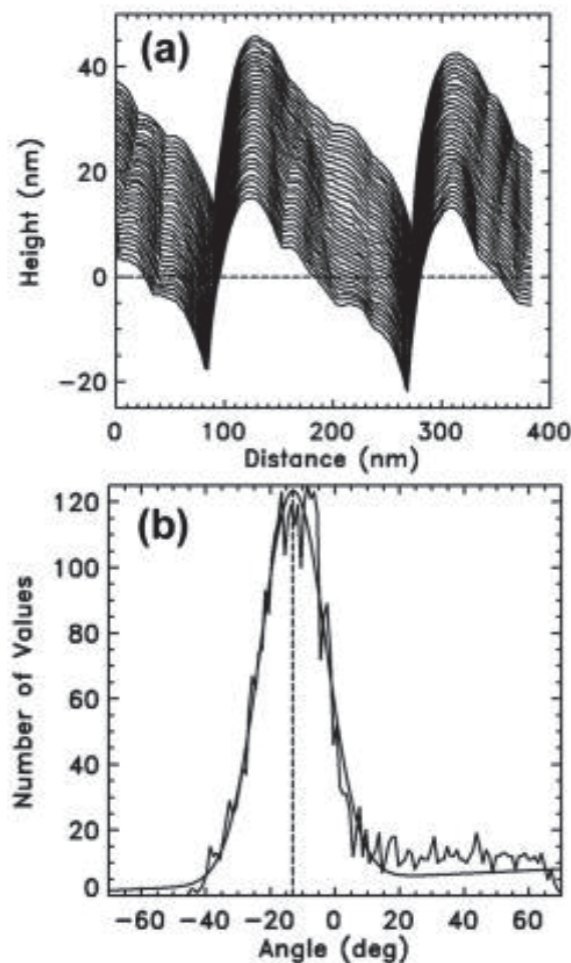


Figure 20.

(a) AFM scans across the grooves near the center of the grating; (b) histogram of the angles of pairs of points on the AFM scans giving a measure of the average blaze angle (after [43]).

The average values of the blaze angles measured at seven points distributed on the grooved area ranged from 8.9° to 15° , and the RMS roughness values ranged from 0.66 to 0.92 nm. Thus, there was considerable variation of the grooves over the 5 cm patterned area. AFM data that were taken before the titanium and gold coating of the imprinted grating showed RMS roughness of approximately 0.2 nm and blaze angles of around 8° , which indicate that deposition of the metal films onto the polymer-based imprint resist led to the observed changes in groove profile [45]. High diffraction efficiencies of the Au-imprinted 5000/mm grating using the average groove profile with 123 nodes of the polygonal groove profile derived from the AFM measurements (**Figure 21**) are demonstrated in Refs [44, 46].

4.5 Si-etched blaze gratings for X-rays: EUV

For medium- and high-frequency diffraction gratings, classical (in-plane) diffraction gives acceptable values of the efficiency of working orders only in the soft X-ray and EUV ranges [47]. However, grazing conical (off-plane) diffraction schemes have great advantages in efficiency when such gratings operate in short-wavelength regions of the X-ray spectrum (hard X-rays and tender X-rays), including in high orders and to obtain high dispersion and resolution. With such a mount, record efficiency, close to that of a respective mirror, can be obtained for sawtooth gratings with blaze angles of several degrees, which are much easier to manufacture. For a theoretical analysis of the diffraction efficiency of such gratings, the use of rigorous electromagnetic theories is required [48, 49].

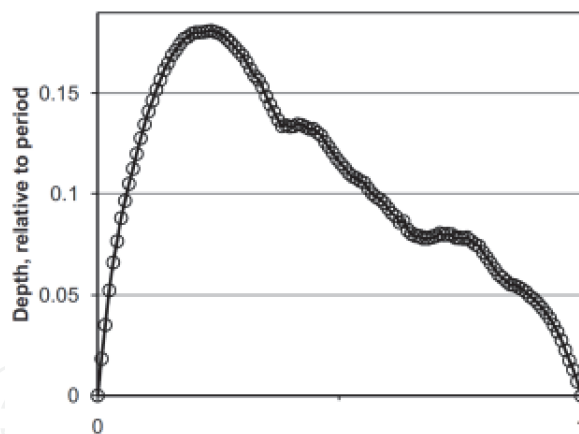


Figure 21.
Normalized average groove profile of an Au-imprinted 5000/mm grating measured by AFM (after [44]).

The manufacturing process of a reflective Si-etched grating of a triangular groove profile (sawtooth or blaze) can be conventionally divided into four main steps: (1) obtaining a pattern of a protective mask for etching grooves (DWL or EBL, in our case); (2) anisotropic etching of grooves in a solution of potassium hydroxide (KOH); (3) etching to smooth the grating profile and polish the surface of the reflective (working) facets; (4) coating to increase reflectivity. In turn, each step consists of several operations that should be controlled using AFM and, if possible, SEM. Some AFM results (NTEGRA Aura microscope) obtained during the grating manufacturing process are considered further in detail.

To transfer the grating pattern directly to a silicon wafer (stage 2), it is etched in KOH with various concentrations at a temperature from room temperature to 50°C with vigorous stirring of the solution [20, 50, 51]. KOH etches the {111} planes more slowly than the rest of silicon, which leads to angular facets with a facet tilt determined by the orientation of the {111} planes relative to the surface plane (i.e., vicinal Si(111) plates). Therefore, KOH etches the pattern of the grooves in the Si while simultaneously setting the blaze angle of grating facets. The author uses here the results of our original Si-etched grating production technique, however, with references to the similar methods for mastering such gratings.

In our AFM studies, the following was performed: measurement of the surface roughness of the working facet on an area of 1×1 and $10 \times 10 \mu\text{m}^2$ and measurement of the grating profile, etching depth and blaze angle of the working facet when scanning $10 \times 10 \mu\text{m}^2$. The measurements were made in the tapping mode using scans of 512×512 pixels. We used TipsNano [4] silicon cantilevers with a typical radius of tips ~ 6 nm. Examples of the AFM topography of Si-etched grating samples with a smoothed profile on the area of 1×1 and $10 \times 10 \mu\text{m}^2$ are shown in **Figure 22a, b** for sample No. 5.

Figure 23a shows the topography profile of specimen No. 5 along line 1 (black curve) and the blaze angle of the working facet (blue curve). The angle is calculated as the arctan of the coordinate derivative and converted to degrees. **Figure 23b** shows the profile of the slope of the non-working facet along line 1 for sample No. 3/1.

The results of AFM studies of the geometrical groove parameters of the samples of Si-etched gratings with a period of $2 \mu\text{m}$ are presented in **Table 5**. In the results presented in **Table 5** the deconvolution algorithms have been used, although we evaluated mid-frequency gratings. The histogram (normalized density of probability) of blaze, anti-blaze, and apex angles of grooves of the grating with 500/mm and 4° blaze angle is demonstrated in **Figure 24** (left). The three peaks on this curve are clearly associated with the corresponding working and non-working facet angles, as well as with the angle of the smoothed top of the groove profile. The average groove

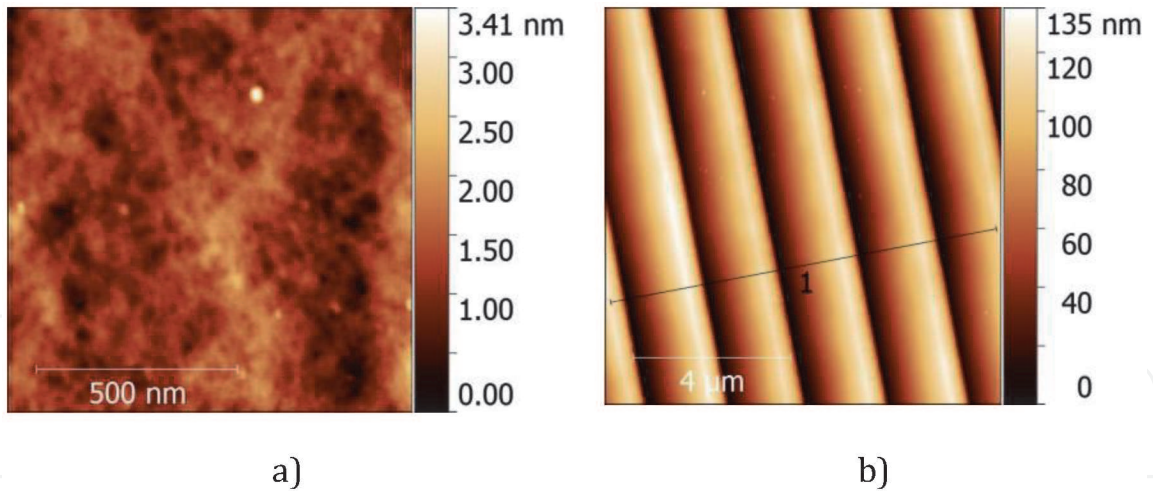


Figure 22.
Surface topography obtained by AFM scanning of area of sample No. 5: a) $1 \times 1 \mu\text{m}^2$; b) $10 \times 10 \mu\text{m}^2$.

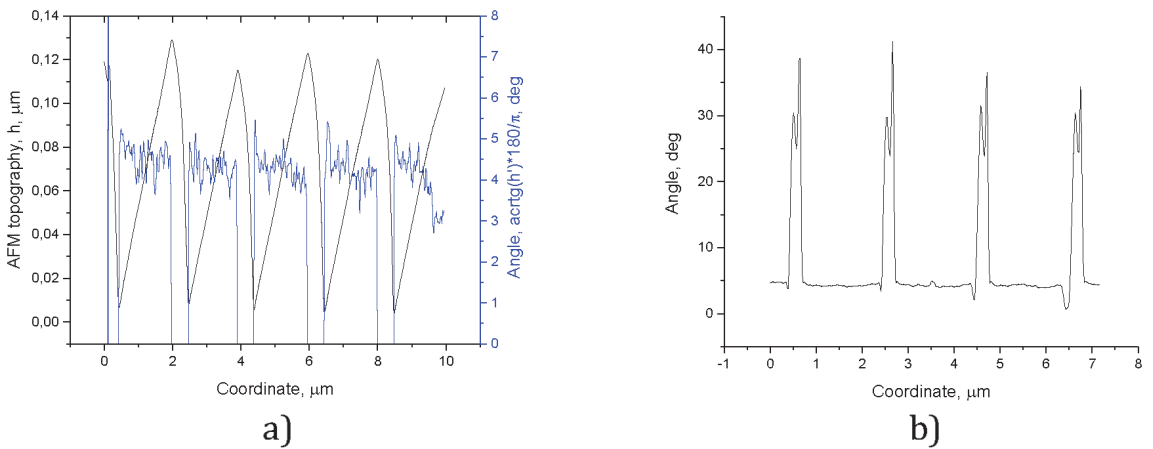


Figure 23.
Profile topography obtained by AFM scanning of area of $10 \times 10 \mu\text{m}$: a) surface and blaze angle of the working facet, sample No. 5; b) anti-blaze angle of the non-working facet, sample No. 3/1.

Sample No.	Groove depth/Si-nub height, nm	Working/non-working facet width, nm	Working facet RMS roughness, nm	Blaze angle, deg.	Anti-blaze angle, deg.
1	95/38	1512/340	0.462	—	—
2	97/44	1544/340	0.345	—	—
3/1	121	1710	0.278	4.05	20
3/2	111	1594	0.340	—	—
5	114	1580	0.337	4.13	20

Table 5.
Groove geometrical parameters of Si-etched grating samples according to AFM.

profile topography and the respective angles one can see in **Figure 24** (right). The peak corresponding to the blaze angle is pronounced and indicates a high quality of the developed sawtooth grating. The average groove profile derived from AFM data for one grating was used then for rigorous calculus of 3D diffraction efficiencies of orders vs. incidence angle and wavelength in the soft-X-ray–EUV range and classical mount (**Figure 25**). The other AFM groove profile data for similar Si-etched

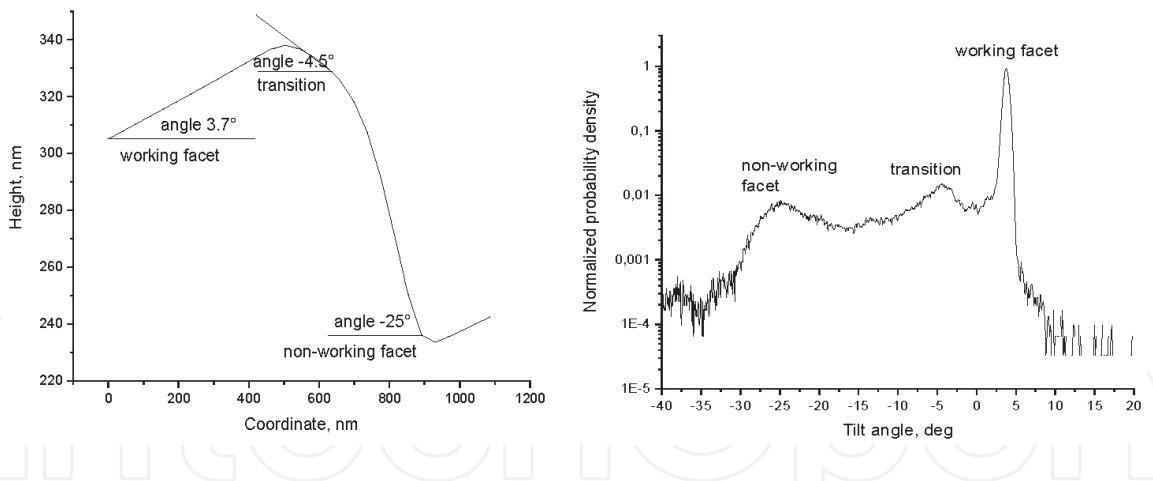


Figure 24. AFM groove parameters of 500/mm and 4° blaze grating: (left) histogram of groove angles including smoothed groove top ('transition'); (right) average groove topography and respective angles.

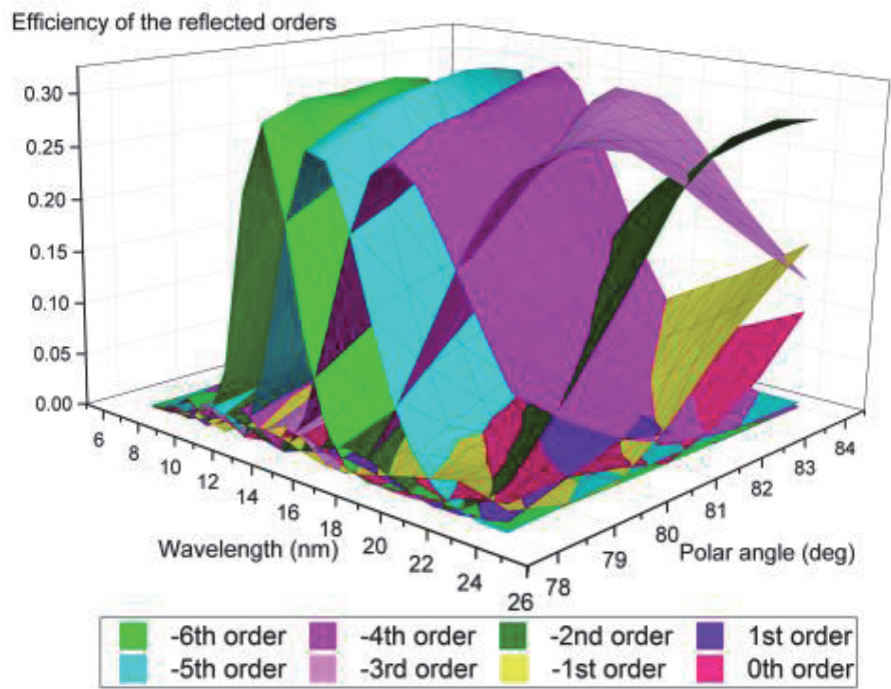


Figure 25. 3D diffraction efficiency in principal orders of 500/mm Au-coated Si-etched grating rigorously calculated using the realistic groove profile vs. incidence angle and wavelength.

gratings produced by DWL, or EBL, or holographic recording can be found in [52, 53] and references there in.

In order to reduce the roughness of the grating surface, the authors of [54] use a nine-cycle RCA-1/HF etching procedure to remove any irregularities and roughness, i.e., perform both smoothing and polishing etching; and they report submicron roughness. To reduce the roughness of the working facet at the polishing stage, several etchants have been tested, including tetramethylammonium hydroxide (TMAH) and the isotropic silicon etchant HF: HNO₃: H₂O. **Table 6** shows the AFM results of processing in different etchants of the surface of samples, punctured from the same grating immediately after anisotropic etching in KOH. As one can see from **Table 6**, the RMS roughness of working facets can be reduced to <0.3 nm for a few etching processes. The initial RMS roughness (before a polishing process) was ~1.2 nm (compare with results in **Table 5**).

Sample No.	Working facet RMS roughness, nm	Polishing etchant/etching time, s
1	0.269	Isotropic/30 s
2	0.244	Isotropic/20 s
3	0.271	Isotropic, using HF before/60 s
4	0.315	Isotropic/60 s
5	0.246	TMAH/2 min
6	0.291	TMAH/4 min
7	0.336	TMAH/6 min
8	0.312	TMAH/8 min
76KDB Si(111)4°- substrate, Ø76.2 mm	0.149	No process

Table 6.
Groove roughness of Si-grating samples according to AFM after polishing.

5. Conclusion

In the chapter, some earlier and recent results of the use of AFM & STM methods for groove metrology of various surface relief (ruled, holographic, lithographic, imprinted) diffraction gratings, mostly intended for short wavelengths, were described and discussed. Examples of a few comparisons with the other widely-used direct metrology techniques, such as SEM, stylus profilometry and microinterferometry, were also demonstrated and compared. In addition, the most critical problems connected with AFM methods for groove metrology of bulk, thin-film-coated and multilayer-coated gratings were discussed, such as: the tip deconvolution and its radius; groove shape and abrupt groove slopes; RMS nano-roughness and PSD functions.

The detailed AFM groove metrology results were presented by the author for several important grating samples: the Space Telescope Imaging Spectrograph grating flown aboard the HST and working in the Visible–NIR; the similar master, replica and multilayer soft-X-ray–EUV blaze gratings; the Cosmic Origins Spectrograph grating used in the last servicing mission to the HST and working in the VUV–NUV; imprinted off-plane blaze grating planned for the International X-ray Observatory and working in the soft X-rays; and recently developed Si-etched blaze diffraction gratings indented to work in the X-rays–EUV at high efficiency and a very low level of scattering light. These gratings were chosen because high quality efficiency data exists, in particular, for space gratings or/and X-ray gratings characterized by synchrotron radiation sources; and their groove profiles, together with random nanoroughness, were measured by AFM to be included in rigorous efficiency and scattered light intensity calculus.

The rigorous calculation accounts for the real profile of the grooves and their thickness as well as suitable refractive indices. It was not possible earlier to achieve such good agreements between measured and calculated efficiencies of high- and mid-frequency gratings working in the short spectral ranges due to the lack of realistic, i.e., measured using the AFM technique, groove profile shapes, as it has been demonstrated in the present study. Today, using an appropriate AFM instrument and the respective method one has a possibility to determine with a superfine (atomic-scale) spatial resolution grating-like structures, i.e., their groove profiles including abrupt slopes and random nanoroughness. Moreover, such

non-destructive AFM analysis is the only suitable one to apply to current production and evaluation of such complicated and expensive devices like as most of X-ray diffraction gratings are.

Acknowledgements

I thank David A. Content, John F. Seely, Tamara N. Berezovskaya, Vladislav A. Sharov for the information provided.

This work was partially supported by the Russian Foundation for Basic Research (RFBR) (Grant No. 20-02-00326) and the Russian Science Foundation (RSF) (Grant No. 19-12-00270) in the theoretical part.

Author details


Leonid I. Goray^{1,2}

1 Alferov University, Saint Petersburg, Russia

2 Institute for Analytical Instrumentation, Saint Petersburg, Russia

*Address all correspondence to: lig@pcgrate.com

IntechOpen

© 2021 The Author(s). Licensee IntechOpen. This chapter is distributed under the terms of the Creative Commons Attribution License (<http://creativecommons.org/licenses/by/3.0>), which permits unrestricted use, distribution, and reproduction in any medium, provided the original work is properly cited. 

References

- [1] Yusupov IY, Mikhailov MD, Herke RR, Goray LI, Mamedov SB, Yakovuk OA. Investigation of the arsenic sulphide films for relief-phase holograms. In: International Seminar on 3D Holography (Three-Dimensional Holography: Science, Culture, Education); 1989, Kiev, Ukraine; Proc SPIE 1238; 1991. p. 240–247. DOI: 10.1117/12.19398
- [2] Palmer C. Diffraction Grating Handbook. 8th ed. MKS Instruments, Inc.; 2020. 250 p.
- [3] Horiba Corp. page. [Internet]. 2021. Available from: <https://www.horiba.com/de/scientific/products/diffraction-gratings/for-scientific-applications/> [Accessed: 2021-02-20]
- [4] TipsNano Co page. [Internet]. 2021. Available from: <https://tipsnano.com/catalog/calibration/> [Accessed: 2021-02-20]
- [5] Helmholtz-Zentrum Berlin page. [Internet]. 2021. Available from: https://www.helmholtz-berlin.de/forschung/oe/wi/praezisionsgitter/index_en.html [Accessed: 2021-02-20]
- [6] Bennett J, Mattson L. Introduction to Surface Roughness and Scattering. 2nd ed. Washington, D.C.: OSA; 1999. 130 p.
- [7] Stout KJ, Blunt L. Three-Dimensional Surface Topography. 2nd ed. Penton Press; 2000. 320 p.
- [8] Scanning Electron Microscopy. Elsevier BV ScienceDirect page. [Internet]. 2021. Available from: <https://www.sciencedirect.com/topics/engineering/scanning-electron-microscopy> [Accessed: 2021-02-20]
- [9] Binnig G, Quate CF, Gerber Ch. Atomic Force Microscope. Physical Review Letters. 1986;56(9):930–933 DOI: 10.1103/PhysRevLett.56.930
- [10] Content DA, Arsenovic P, Kuznetsov IG, Hadjimichael T. In: International Symposium on Optical Science and Technology (Optical Spectroscopic Techniques, Remote Sensing, and Instrumentation for Atmospheric and Space Research IV); 2001, San Diego, CA, United States; Proc SPIE 4485; 2002. p. 405–416. DOI: 10.1117/12.454276
- [11] Goray L, Jark W, Eichert D. Rigorous calculations and synchrotron radiation measurements of diffraction efficiencies for tender X-ray lamellar gratings: conical versus classical diffraction. J Synchrotron Rad. 2018;25:1683–1693. DOI: 10.1107/S1600577518012419
- [12] MicroXAM. Phase Shift Technology, Inc. instrument specification. [Internet]. 2002. Available from: <https://www.ccmr.cornell.edu/wp-content/uploads/sites/2/2015/11/MicroXam-specs.pdf> [Accessed: 2021-02-20]
- [13] KLA-Tencor P-10 Surface Profiler. ClassOne Equipment, Inc. page [Internet]. 2021. Available from: <https://classoneequipment.com/product/kla-tencor-p-10-surface-profiler-2/> [Accessed: 2021-02-20]
- [14] XP-S Stylus Profiler. Ambios Technology, Inc. instrument specification. [Internet]. 2021. Available from: http://cloudfront.eas.caltech.edu/a-phms/research/facilities/micro_nano/documents/micro-nano-profilometer-user-manual.pdf [Accessed: 2021-02-20]
- [15] NanoScope III SPM System. Digital Instruments, Inc. instrument specification. [Internet]. 2021. Available from: http://www.photonicmicrodevices.com/files/Digital_Instruments_Nanoscope_General_Description_and_Specs.pdf [Accessed: 2021-02-20]
- [16] NTEGRA-Aura SPM. NT-MDT BV page. [Internet]. 2021. Available from:

<https://ntmdt.nl/home/products/integra-aura/> [Accessed: 2021-02-20]

[17] Carl-Zeiss Supra 25 SEM. EVISA page. [Internet]. 2010. Available from: <http://www.speciation.net/Database/Instruments/Carl-Zeiss-AG/Supra-25-i665> [Accessed: 2021-02-20]

[18] VLSI standards. VLSI page. [Internet]. 2021. Available from: <https://www.vlsistandards.com/products/overview.asp> [Accessed: 2021-02-20]

[19] Herada T, Taira E, Kita T, Itou M. Groove Profile Measurement of Diffraction Gratings Using Scanning Electron Microscope. In: 31st Annual Technical Symposium on Optical and Optoelectronic Applied Sciences and Engineering (Application and Theory of Periodic Structures, Diffraction Gratings, and Moire Phenomena III); 1987, San Diego, CA, United States; Proc SPIE 0815; 1987. DOI: 10.1117/12.941742

[20] Voronov DL, Ahn M., Anderson EH, Cambie R, Chang C-H, Goray LI, Gullikson EM, Heilmann RK, Salmassi F, Schattenburg ML, Warwick T, Yashchuk VV, Padmore HA. High efficiency multilayer blazed gratings for EUV and soft X-rays: Recent developments. In: SPIE Optical Engineering + Applications (Advances in X-Ray/EUV Optics and Components V); 2010, San Diego, CA, United States; Proc SPIE 7802; 2010. p. 780207. DOI: 10.1117/12.861287

[21] Canet-Ferrer J, Coronado E, Forment-Aliaga A, Pinilla E. Correction of the tip convolution effects in the imaging of nanostructures studied through scanning force microscopy. *Nanotechnology*. 2014;25(39):395703. DOI: 10.1088/0957-4484/25/39/395703

[22] Vorselen D, Kooreman E, Wuite G, Roos WH. Controlled tip wear on high roughness surfaces yields gradual broadening and rounding of cantilever tips. *Sci Rep*. 2016;6:36972 DOI: 10.1038/srep36972

[23] Andrie A, Hönicke P, Gwalt G, Schneider P-I, Kayser Y, Siewert Frank, Soltwisch V. Shape- and element-sensitive reconstruction of periodic nanostructures with grazing incidence X-ray fluorescence analysis and machine learning. *arXiv.org*. 2021, 12 Feb; arXiv:2102.06600v1 [physics.app-ph]

[24] Garnæs P-E, Hansen NA, Holm J, Borsetto F, Kühle A. Profiles of a high-aspect-ratio grating determined by spectroscopic scatterometry and atomic-force microscopy. *Applied Optics*. 2006; 45(14):3201–3212.

[25] Kondratov AV, Rogov OY, Gainutdinov RV. AFM reconstruction of complex-shaped chiral plasmonic nanostructures. *Ultramicroscopy*. 2017; 181,81–85. DOI: doi.org/10.1016/j.ultramic.2017.05.013

[26] Goray L, Lubov M. Analysis of mirror soft-x-ray–EUV scattering using generalized continuous growth model of multiscale reliefs. *Optics Express*. 2015; 23(8):10703–10713

[27] Church EL, Takacs PZ. Surface Scattering. In: Bass M, editor. *Handbook of Optics: Volume I – Geometrical and Physical Optics, Polarized Light, Components and Instruments*. 3rd ed. McGraw-Hill; 2010. Ch. 8

[28] Content DA, Boucarut RA, Bowers CW, Madison TJ, Wright GA, Lindler DJ, Huang LK, Puc BP, Standley C, Norton TA. Development and testing of diffraction gratings for the Space Telescope Imaging Spectrograph. In: SPIE's 1996 International Symposium on Optical Science, Engineering, and Instrumentation (Space Telescopes and Instruments IV); 1996, Denver, CO, United States; Proc SPIE 28074; 1996. p. 267. DOI: 10.1117/12.255105

[29] International Intellectual Group, Inc page. [Internet]. 2021. Available from:

https://www.pcgrate.com/etestlab/certific/index_html#9 [Accessed: 2021-02-20]

[30] Kowalski MP, Seely JF, Goray LI, Hunter WR, Rife JC. *Applied Optics*. 1997;36(34):8939–8943. DOI: 10.1364/AO.36.008939

[31] Seely JF, Goray LI, Hunter WR, Rife JC. *Applied Optics*. 1999;38(7):1251–1258. DOI: 10.1364/AO.38.001251

[32] Topometrics Explorer Scanning Probe Microscope. MIT page. [Internet]. 1997. Available from: <http://electron.mit.edu/~gsteele/mirrors/elchem.kaist.ac.kr/jhkwak/TopometrixWeb/Explorer.htm> [Accessed: 2021-02-20]

[33] Seely JF, Kowalski MP, Cruddace RG, Heidemann KF, Heinzmann U, Kleineberg U, Osterried K, Menke D, Rife JC, Hunter WR. Multilayer-coated laminar grating with 16% normal-incidence efficiency in the 150-Å wavelength region. *Applied Optics*. 1997;36(31):8206–8213. DOI: 10.1364/AO.36.008206

[34] Kowalski MP, Barbee TW, Heidemann KF, Gursky H, Rife JC, Hunter WR, Fritz GG, Cruddace RG. Efficiency calibration of the first multilayer-coated holographic ion-etched flight grating for a sounding rocket high-resolution spectrometer. *Applied Optics*. 1999;38(31):6487–6493 (1999). DOI: 10.1364/AO.38.006487

[35] Goray LI, Seely JF. Efficiencies of master, replica, and multilayer gratings for the soft-x-ray-extreme-ultraviolet range: modeling based on the modified integral method and comparisons with measurements. *Applied Optics*. 2002;41(7):1434–1445. DOI: 10.1364/AO.41.001434

[36] Seely JF, Montcalm C, Baker S, Bajt S. High-efficiency MoRu–Be multilayer-coated gratings operating near normal incidence in the 11.1–12.0-

nm wavelength range. *Applied Optics*. 2001;40(31):5565–5574. DOI: 10.1364/AO.40.005565

[37] Goray LI, Keznetsov IG, Sadov SYu, Content DA. Multilayer resonant subwavelength gratings: effects of waveguide modes and real groove profiles. *JOSA A*. 2006;23(1):155–165. DOI: 10.1364/JOSAA.23.000155

[38] Green JC. Cosmic origins spectrograph. In: *Astronomical Telescopes and Instrumentation (UV, Optical, and IR Space Telescopes and Instruments)*; 2000, Munich, Germany; Proc SPIE 4013; 2000. p. 352. DOI: 10.1117/12.394017

[39] Kuznetsov IG, Wilkinson E, Content DA, Boucarut RA, Madison TJ, In: *Optical Science and Technology, SPIE's 48th Annual Meeting (Optical Modeling and Performance Predictions)*; 2003, San Diego, California, United States; Proc SPIE 5178; 2004. p. 267. DOI: 10.1117/12.507946

[40] International Intellectual Group, Inc page. [Internet]. 2021. Available from: https://www.pcgrate.com/load_purc/download/ [Accessed: 2021-02-20]

[41] Palik E, editor. *Handbook of optical constant of solids, II, III*. New York: Academic Press; 1985, 1991, 1998.

[42] NASA IXO page [Internet]. 2021. Available from: <https://asd.gsfc.nasa.gov/archive/ixo/technology/xgs.html> [Accessed: 2021-02-20]

[43] Seely JF, Goray LI, Kjornrattanawanich B, Laming JM, Holland GE, Flanagan KA, Heilmann RK, Chang C-H, Schattenburg ML, Rasmussen AP. Efficiency of a grazing incidence off-plane grating in the soft x-ray region. *Applied Optics*. 2006;45(8):1680–1687. DOI: 10.1364/AO.45.001680

- [44] Goray LI, Schmidt G. Solving conical diffraction grating problems with integral equations. *J. Opt. Soc. Am. A.* 2010;27(3): 585–597. DOI: 10.1364/AO.45.001680
- [45] Chang C-H, Montoya JC, Akilian M, Lapsa A, Heilmann RK, Schattenburg ML, Li M, Flanagan KA, Rasmussen AP, Seely JF, Laming JM, Kjornrattanawanich B, Goray LI. High fidelity blazed grating replication using nanoimprint lithography. *J Vac Sci Technol B.* 2004;22:3260–3264. DOI: 10.1116/1.1809614
- [46] Goray LI, "Off-plane grazing-incidence fan-groove blazed grating to serve as a high-efficiency spectral purity filter for EUV lithography. In: *SPIE Optics + Photonics, Components, and Applications (Advances in X-Ray/EUV Optics)*; 2006, San Diego, CA, United States; Proc SPIE 6317; 2006. p. 631700. DOI: 10.1117/12.678151
- [47] Goray L, Jark W, Eichert D. Rigorous calculations and synchrotron radiation measurements of diffraction efficiencies for tender X-ray lamellar gratings: conical versus classical diffraction. *J Synchrotron Rad.* 2018;25: 1683–1693. DOI: 10.1107/S1600577518012419
- [48] Popov E, editor. *Gratings: Theory and Numeric Applications*. 2nd rev. ed. AMU Press; 2014. Ch. 12
- [49] Voronov DL, Goray LI, Warwick T, Yashchuk VV, Padmore HA. High-order multilayer coated blazed gratings for high resolution soft x-ray spectroscopy. *Optics Express.* 2015;23(4):4771–4790. DOI: 10.1364/OE.23.004771
- [50] Voronov DL, Anderson EH, Cambie R, Salmassi F, Gullikson EM, Yashchuk VV, Padmore HA, Ahn M, Chang C, Heilmann RK, Schattenburg ML. 5000 groove/mm multilayer-coated blazed grating with 33% efficiency in the 3rd order in the EUV wavelength range. In: *SPIE Optical Engineering + Applications (Advances in X-Ray/EUV Optics and Components IV)*; 2009, San Diego, California, United States; Proc SPIE 7448; 2009. p. 74480J. DOI: 10.1117/12.826921
- [51] Ahn M, Heilmann RK, Schattenburg ML. Fabrication of ultrahigh aspect ratio freestanding gratings on silicon-on-insulator wafers. *J Vac Sci Technol B.* 2007;25(6):2593–2597. DOI: 10.1116/1.2779048
- [52] Voronov DL, E.H. Anderson, Cambie R, Cabrini S, Dhuey SD, Goray LI, Gullikson EM, Salmassi F, Warwick T, Yashchuk VV, Padmore HA. A 10,000 groove/mm multilayer coated grating for EUV spectroscopy. *Optics Express.* 2011;19(7):6320–6325. DOI: 10.1364/OE.19.006320
- [53] Voronov DL, Anderson EH, Cambie R, Goray LI, Gawlitza P, Gullikson EM, Salmassi F, Warwick T, Yashchuk VV, Padmore HA. Development of near atomically perfect diffraction gratings for EUV and soft x-rays with very high efficiency and resolving power. *Journal of Physics: C.* 2013;425:152006. DOI: 10.1088/1742-6596/425/15/152006
- [54] Golub L, Cheimets P, DeLuca EE, Madsen CA, Reeves KK, Samra J, Savage S, Winebarger A, Bruccoleri AR. EUV imaging and spectroscopy for improved space weather forecasting. *J Space Weather Space Clim.* 2020;10:37 DOI: 10.1051/swsc/2020040